Electronic Supplementary Material (ESI) for Energy & Environmental Science.

Supplementary Information

Tailoring surface cation configuration of Ruddlesden-Popper perovskites for controllable water oxidation performance

Yu Li, Gao Chen, Hsiao-Chien Chen, Yanping Zhu, Liangshuang Fei, Longwei Xu, Tiancheng Liu, Jie Dai, Haitao Huang, Wei Zhou,* and Zongping Shao**

Experimental Procedures

Synthesis of L_2N and LSNF samples. L_2N were synthesized by a typical sol-gel method. For example, 43.3 g $La(NO_3)_3 \cdot 6H_2O$ and 14.5405 g $Ni(NO_3)_2 \cdot 6H_2O$ (all of analytical grade, Sinopharm Chemical Reagent Co., Ltd.) were dissolved in deionized water. Then, a mixed Ethylenediamine tetraacetic acid (EDTA, $C_{10}H_{16}N_2O_8$, 43.836 g) and Citric acid monohydrate (CA, $C_6H_8O_7$, 63.042 g) solution were added to form a molar ratio of 1:2:1 for the metal ions/CA/EDTA. Next, an aqueous ammonium hydroxide solution ($NH_3 \cdot H_2O$, 28%) was added to adjust the pH to approximately 6. The mixed solution was then heated at 90 °C until it formed a gel. We then put the gel in the oven for 5 hours. Finally, the obtained precursor was put into a 1000 °C muffle furnace for 5 h to obtain the perovskite powder. LSNF was synthesized via the same process above except the different stoichiometric amounts. The dissolution process took place in a quartz beaker.

Synthesis of L_2N@NF samples. Firstly, the obtained L_2N powders were grounded by ball-milling for 1 hour. Then, we added 0.075g $FeCl_3 \cdot 6H_2O$ into 30 ml deionized water to form a solution (~ 0.01 M). 0.2g grounded L_2N was then added into it. The suspension liquid was then placed in an ultrasonic cell disruptor for half an hour. After the end of it, the product was washed several times with deionized water by centrifugation. The obtained product was placed in the oven to dry. Next, we make the $FeCl_3 \cdot 6H_2O$ solution 30 ml again with 0.05g $FeCl_3 \cdot 6H_2O$ and added the dried product into it with the ultrasonic assisted for 30 minutes. Finally, the obtained L_2N@NF powders were washed with ultrapure water by centrifugation and dried.

Synthesis of $L_2N@NF_x$ ($L_2N@NF_{0.51}$, $L_2N@NF_{0.78}$, $L_2N@NF_{1.63}$, and $L_2N@NF_{1.99}$) samples. The steps for synthesis are the same as L_2N@NF, except for $FeCl_3$ solution concentration. Briefly, 0.03g, 0.05g, 0.11g, and 0.2g $FeCl_3 \cdot 6H_2O$ were added separately to 30 ml deionized water to form the solution and then 0.2g grounded L_2N was added to them for 0.5 h. After several centrifuges, the products were transferred to 30 ml aqueous solution containing 0.05g $FeCl_3 \cdot 6H_2O$ for 30 minutes again with the ultrasonic assisted. Finally, the obtained $L_2N@NF_{0.51}$, $L_2N@NF_{0.78}$, $L_2N@NF_{1.63}$ and $L_2N@NF_{1.99}$ samples were centrifuged and dried. The x here stand for the value of (Ni+Fe)/La. According to the pH meter test, solutions of 0.03g, 0.05g, 0.075g, 0.11g and 0.2g $FeCl_3 \cdot 6H_2O$ dissolved in 30 ml deionized water have pH values of 2.74, 2.61, 2.53, 2.48 and 2.38, respectively.

Synthesis of L_2N-Fe samples. L_2N-Fe was synthesized by introducing Fe during the L_2N electrochemical testing. Firstly, 0.1 M aqueous $Fe(NO_3)_3$ solution was prepared from $Fe(NO_3)_3 \cdot 9H_2O$ and ultrapure water. Then, adding 0.08 ml of 0.1 M $Fe(NO_3)_3$ solution into the 100 ml of 1.0 M KOH electrolyte. Continuous linear voltammetry scanning until performance no longer changes. According to the calculation, the pH of the electrolyte is almost unchanged.

Materials characterization. The XRD patterns of samples were obtained from the X-ray powder diffractometer (Rigaku Smartlab, Cu Kα radiation, λ =1.5418 Å). FESEM (HITACHI S-4800) was used to conduct the morphologies of the catalysts and TEM (FEI Tecnai G2 T20) was used to get the lattice parameters equipped with a Philips Tecnai T30F field emission instrument. Desorption curve and pore size distribution were obtained with a Brunauer-Emmett-Teller (BET) analysis system with a N_2 adsorptive medium. The valence state and content of the elements was obtained with the XPS (PHI550). The 4d orbitals of La, 3p orbitals of Ni and 2p orbitals of Fe were tested to determine the content of surface elements. The XAS spectra were collected in total-fluorescence-yield mode at ambient air in BL-12B2 at SPring-8, JARSI.

Electrode preparation and electrochemical characterization. Electrochemical properties and the

electrochemical oxygen intercalation were tested in an O_2-saturated and argon-saturated 1.0 M KOH solution, respectively. The glassy carbon electrode (PINE, 5 mm diameter, 0.196 cm^2) was used as the working electrode and the Hg/HgO electrode as the reference electrode. Carbon rods serve as counter electrodes. The glassy carbon electrode is supported with catalysts and connected to a CHI 760E electrochemistry electrochemical station. 10 mg catalyst, 10 mg super P, 1 mL anhydrous ethanol, and 100 μL Nafion were mixed and ultrasonic for 30 min. Spread 5 μL ink evenly on the glassy carbon electrode. LSV was performed from 0.2 V to 1 V versus Hg/HgO at the RDE at 1600 rpm with a sweep rate of 5 mV s^{-1}. 1 mg catalyst and 0.1 mg Super P were uniformly loaded on the 1 cm × 1 cm carbon paper to test the stability. Electrochemical oxygen insertion and extraction test was performed at a scan rate of 20 mV s^{-1} between -0.2 V and 0.6 V versus Hg/HgO. To obtain the specific oxidative charge from the integration of oxidation waves, the baseline of each cyclic voltammetry (CV) was fit and subtracted from the specific current density. Oxygen ion diffusion coefficient was performed with the chronoamperometry. A potential of more than $E_{1/2}$ (defined as the potential halfway between the peak currents for oxygen insertion and extraction) 50 mV is applied to the working electrode to obtain chronoamperometry data. The measured data were plotted as current versus the inverse square root of time (i vs. $t^{-1/2}$), in which a linear regression was used to obtain the intercept with the $t^{-1/2}$ axis (at i = 0). According to the equation $\lambda = a(D_o t)^{-1/2}$, the oxygen ion diffusion coefficient (D_o) can be calculated. Here, λ is a dimensionless shape factor and was assumed to be 2. a need to be estimated with the relation of S = 6/(2aρ), where S is the BET specific surface area and ρ is the theoretical density which can be obtained from the Rietveld analysis. Turnover frequency (TOF) was investigated via the following equation：

$$Turnover\ frequency\ (TOF) = \frac{j}{n \times F \times N_s}$$

Where j is the current, n is the number of electrons transferred to evolve a molecule of the product (for H_2 and O_2, n is 2 or 4), F is Faradaic constant and N_s is the number of moles of active sites available for the catalysis. S-number was calculated via following equation:

$$S - number = \frac{n(O_2)}{n(dissolved\ Ni)}$$

The amount of produced oxygen was calculated from total charge and the dissolved iridium was obtained from ICP-MS results.

Isotope-Labeled Method. Firstly, A carbon paper with catalysts (2 mg cm^{-2}) was activated in ^{18}O labeled 1.0 M KOH for 10 min at 10 mA cm^{-2}. Then, the carbon paper was carefully washed with $H_2{}^{16}O$ deionized water to remove surface $H_2{}^{18}O$. Finally, the carbon paper was measured for three CV cycles in 1.0 m KOH with $H_2{}^{16}O$. The CV test was performed at a scan rate of 4 mV s^{-1} between 0 V and 0.7 V versus Ag/AgCl. All the tests were carried out in an H-cell. The gaseous products from the anode side were analyzed by mass spectrometry.

MEA electrolyser system. The AEM water electrolyzer included the anode (L_2N@NF and IrO_2), cathode (commercial Pt/C, 20 wt% Pt), gas diffusion layer (Ni foam), and anion exchange membrane (Sustainion X37-50 Grade RT). The L_2N@NF was mixed with Super P with a weight ratio of 4:1. The obtained powder was then added into the liquid with 1 ml anhydrous ethanol and 100 μl nafion. After the ultrasound, the ink was sprayed on the Ni foam. The electrode area of anode and cathode is 4 cm^2 (2 cm*2 cm), and the effective electrode area of the anode is 1 cm^2 (1 cm*1 cm). In other words, anode catalysts are only sprayed in the central 1 cm*1 cm area. The catalyst loading amount for the anode is 3 mg cm^{-2} and 1 mg_{Pt} cm^{-2} for the cathode. All catalysts were sprayed on a gas diffusion layer using an ultrasonic spray machine. The AEM water electrolyzer was connected with a digital source meter (Keithley 2420). 1 M KOH was pumped into the electrolyzer with a peristaltic pump and formed a cycle. The

durability testing of AEM water electrolyzer was conducted at 60 ˚C at the current density of 200 mA cm^{-2}. The membrane was changed every 100 h for L_2N@NF.

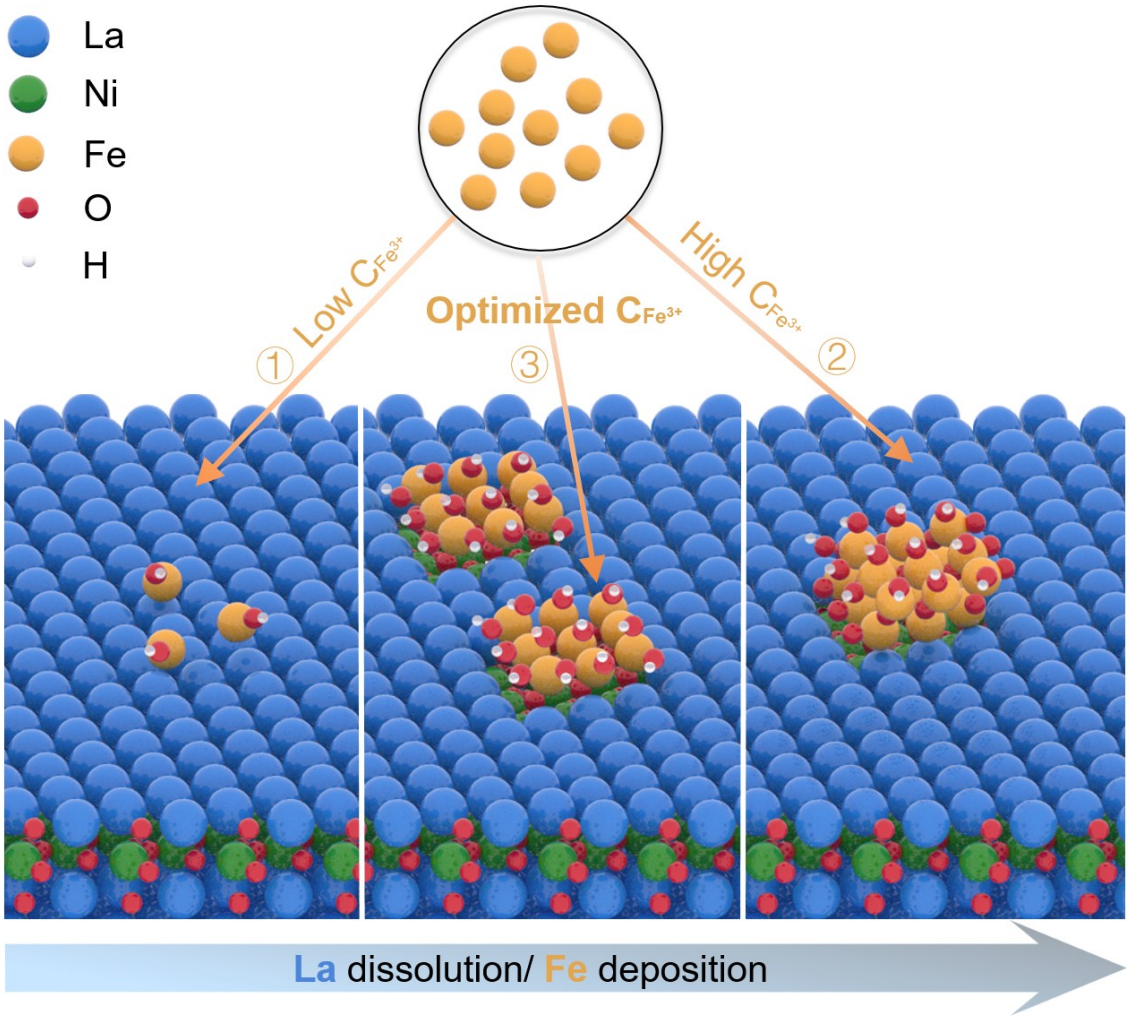

Figure S1. Three typical surface cation configurations under different concentration of $FeCl_3$ solution. (Left) Low-concentration $FeCl_3$ solution leads to the residual of inert La, which hinders the formation of Ni-Fe pairs. (Right) Excessive Fe^{3+} ions are deposited on the surface of L_2N@NF, burying the subsurface Ni-Fe pairs. (Middle) Optimized-concentration of Fe^{3+} ions yield the dissolution of La and formation of Ni-Fe pairs on the surface.

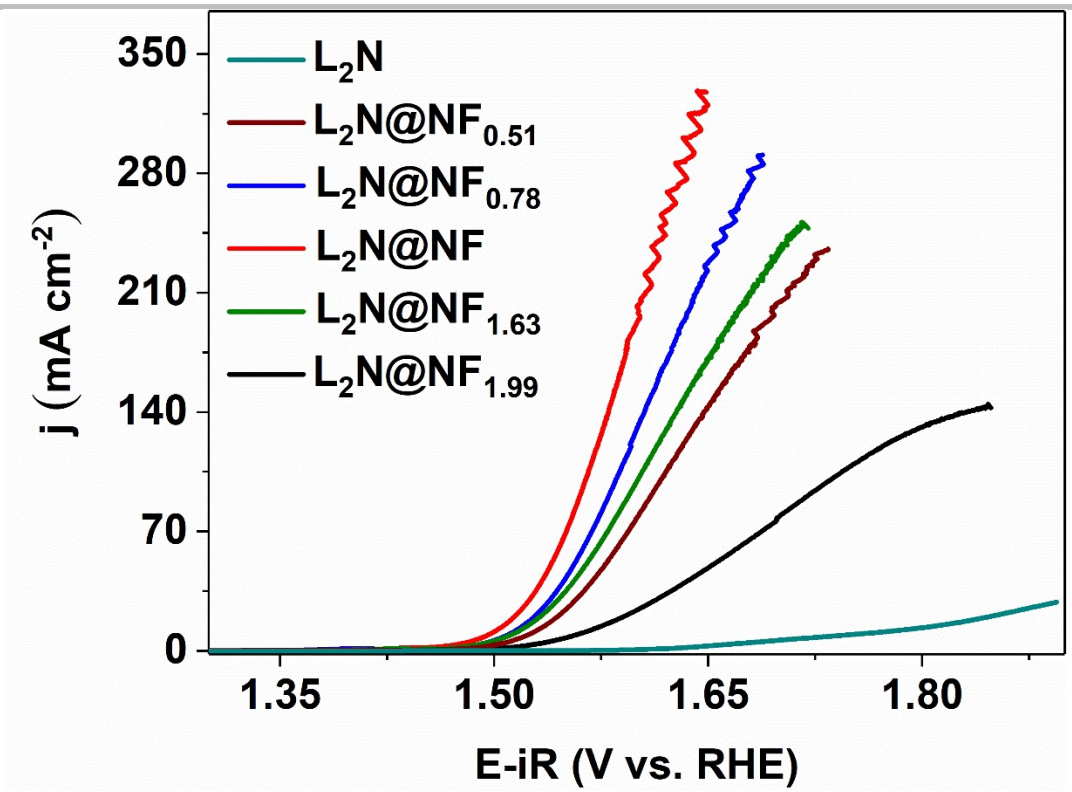

Figure S2. OER activity of pristine L_2N and L_2N after a series of $FeCl_3$ solutions with varying concentrations ($L_2N@NF_x$). L2N@NF exhibited the best OER activity among the $L_2N@NF_x$ catalysts.

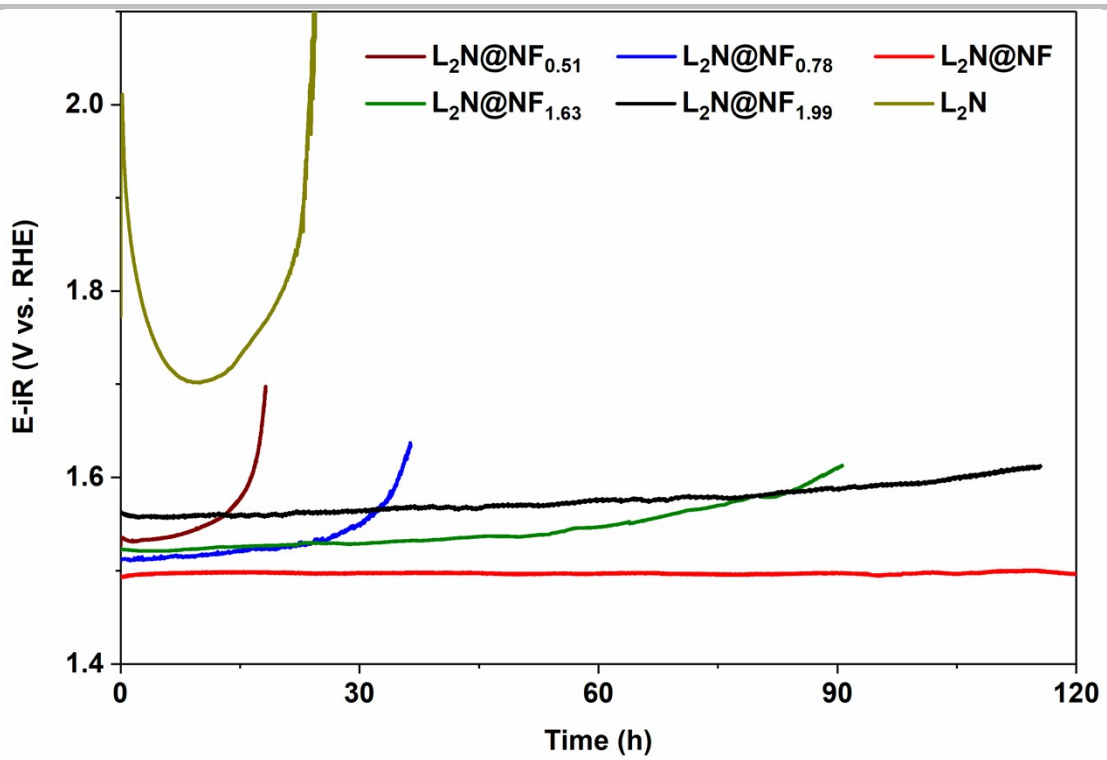

Figure S3. OER stability of pristine L_2N and L_2N after a series of $FeCl_3$ solutions with varying concentrations ($L_2N@NF_x$).

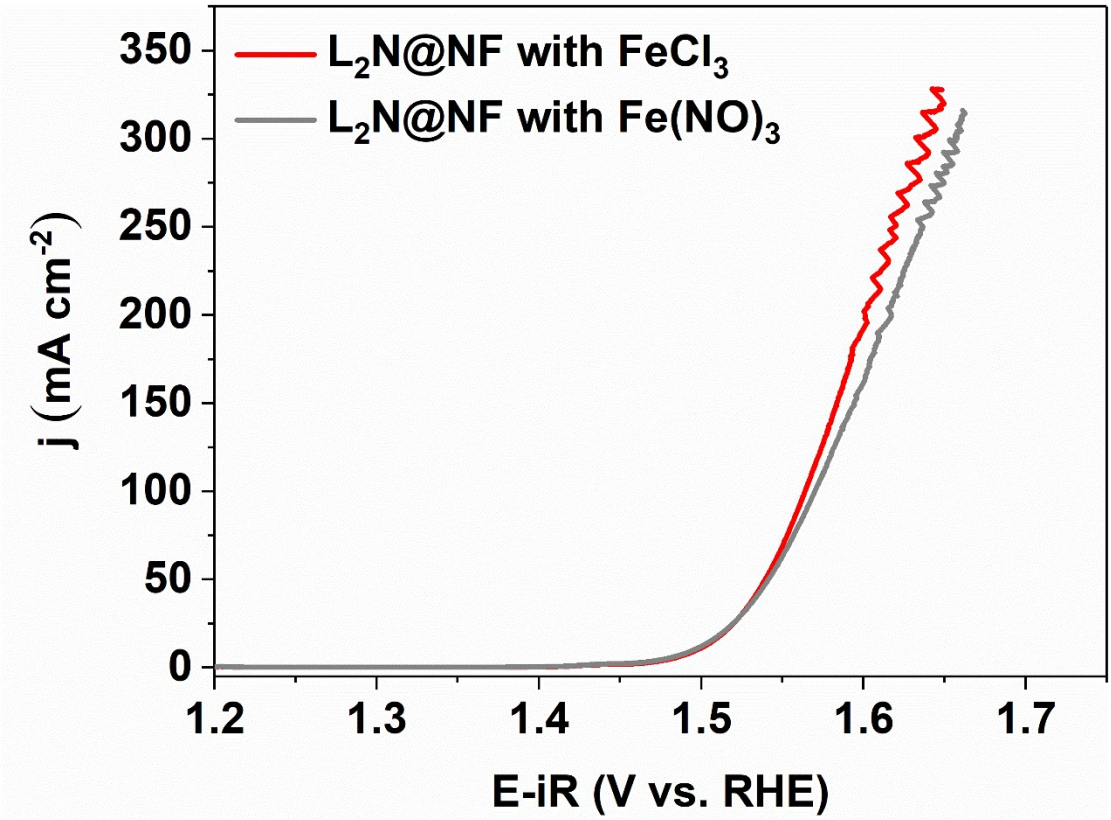

Figure S4. OER performance. The OER performance of $L_2N@NF$ treated with the same concentration of $FeCl_3$ solution and $Fe(NO)_3$ solution.

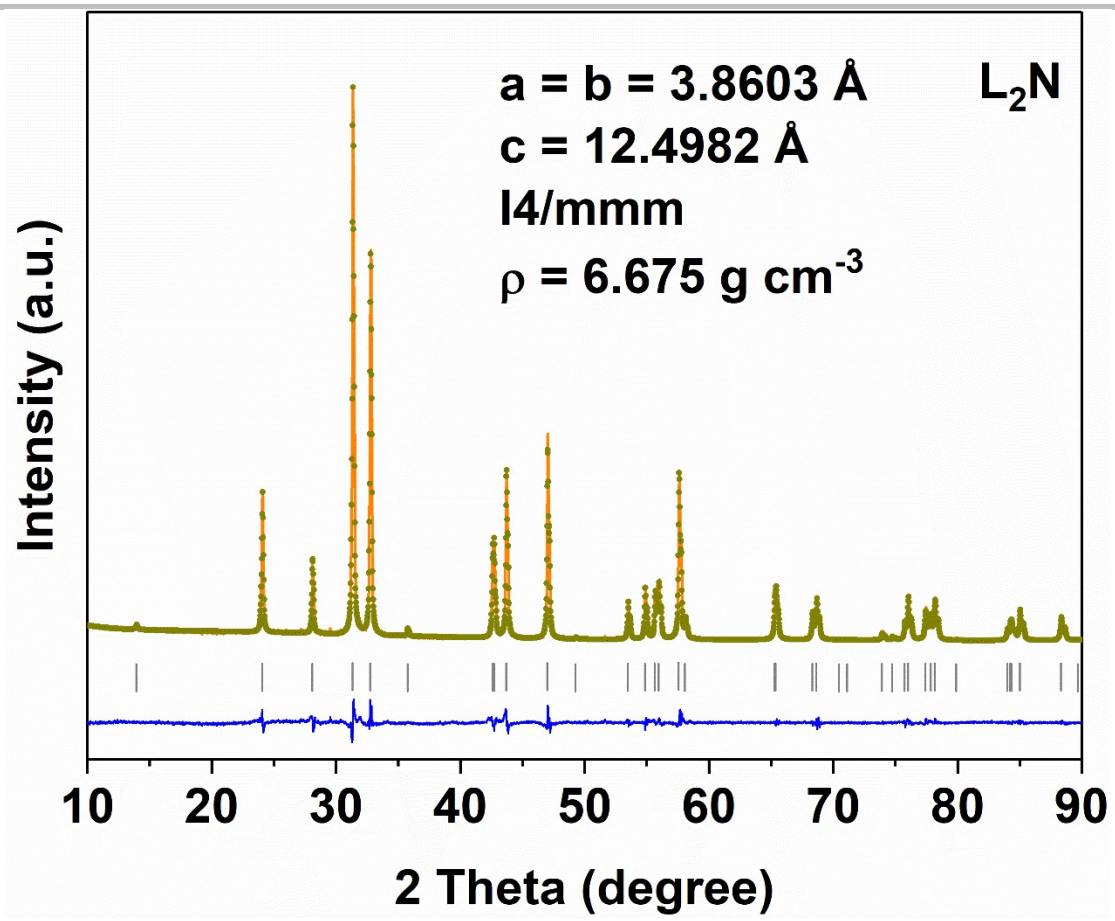

Figure S5. Rietveld refinement patterns. XRD refinement of the L_2N.

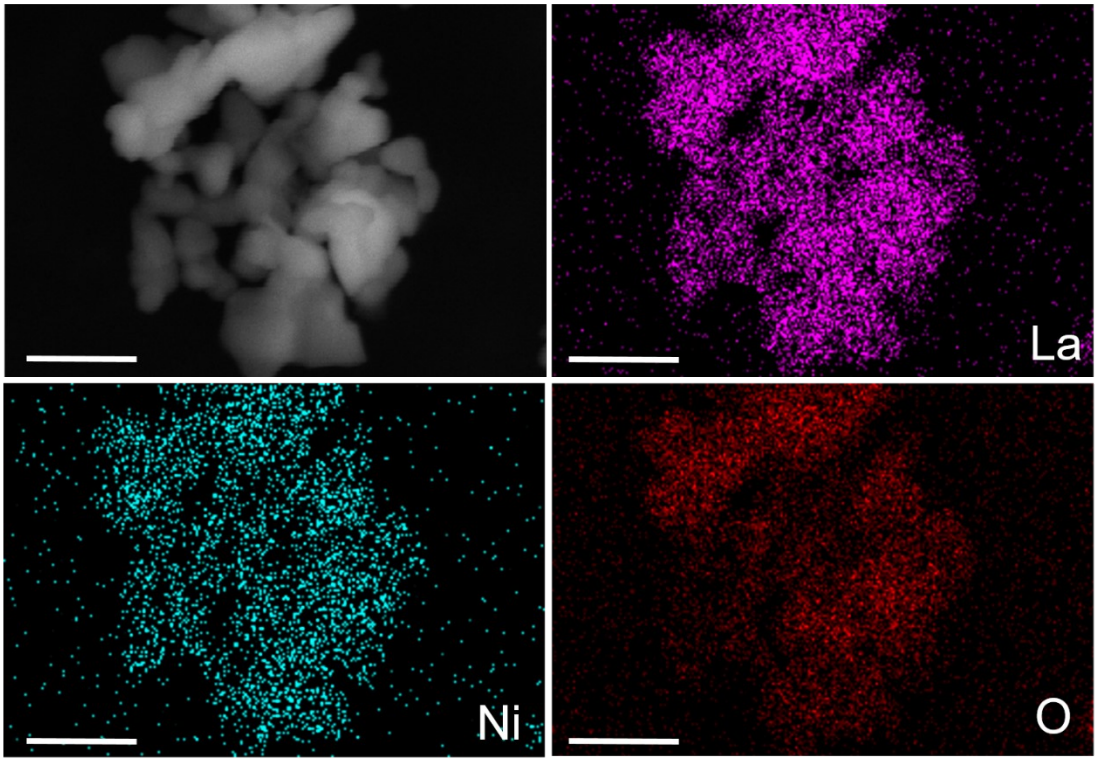

Figure S6. Elemental mappings. The elemental mappings of L_2N. The scale bar is 500 nm.

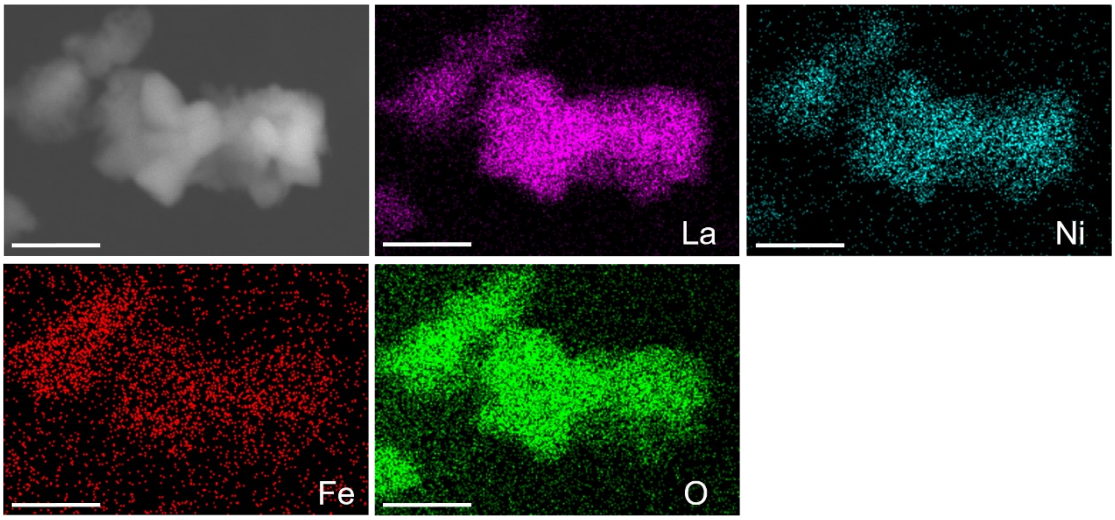

Figure S7. Elemental mappings. The elemental mappings of L_2N@NF. The scale bar is 500 nm.

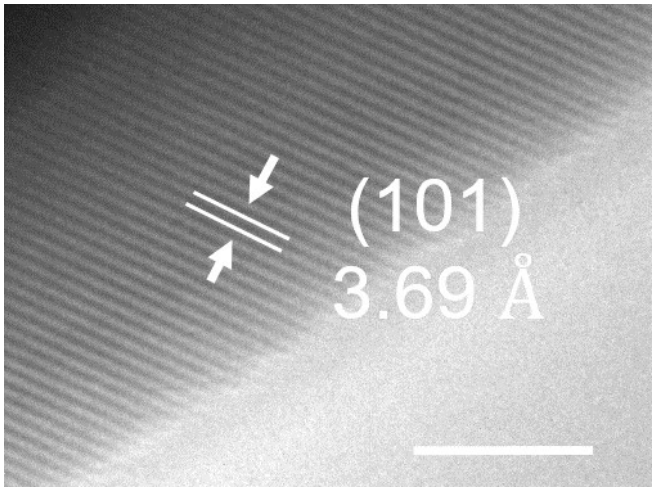

Figure S8. TEM image of L_2N. The scale bar is 5 nm.

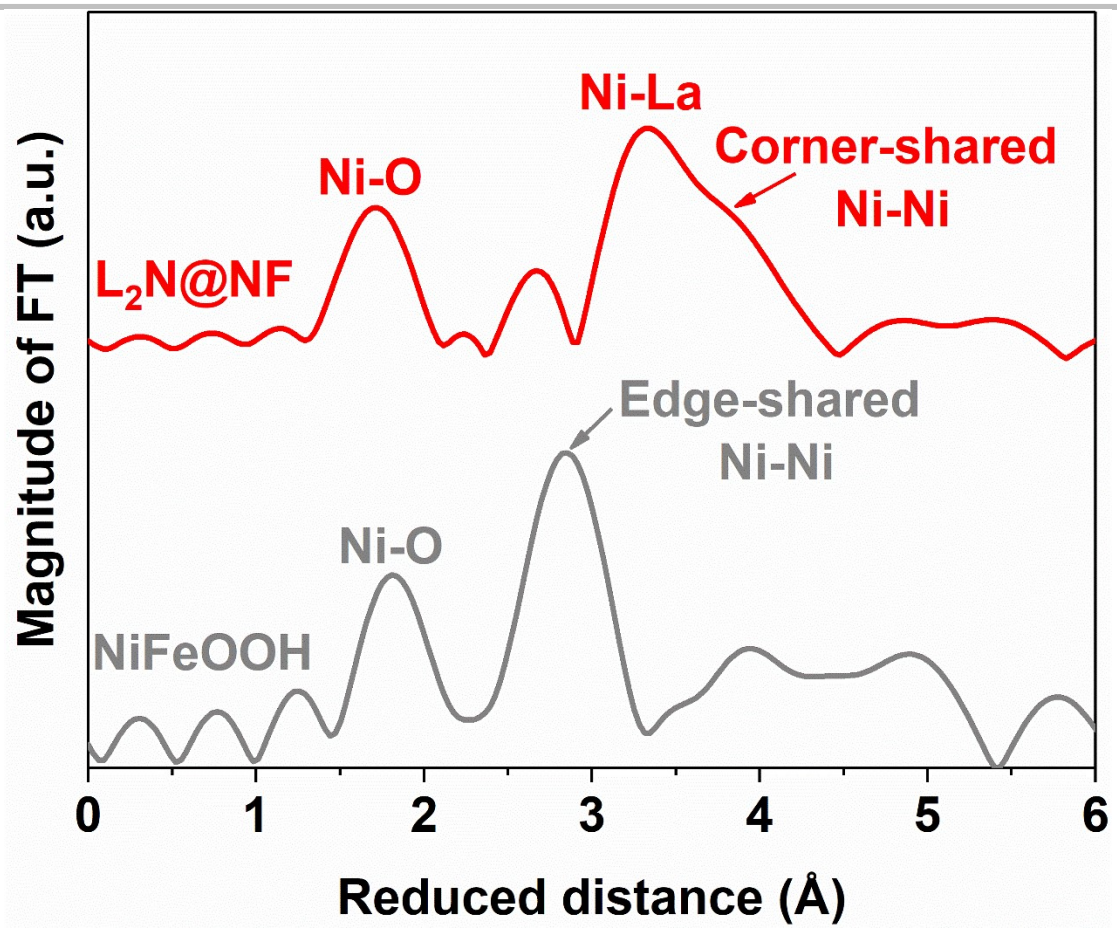

Figure S9. Fourier transform EXAFS. Ni K-edges EXAFS of L_2N@NF and NiFeOOH.

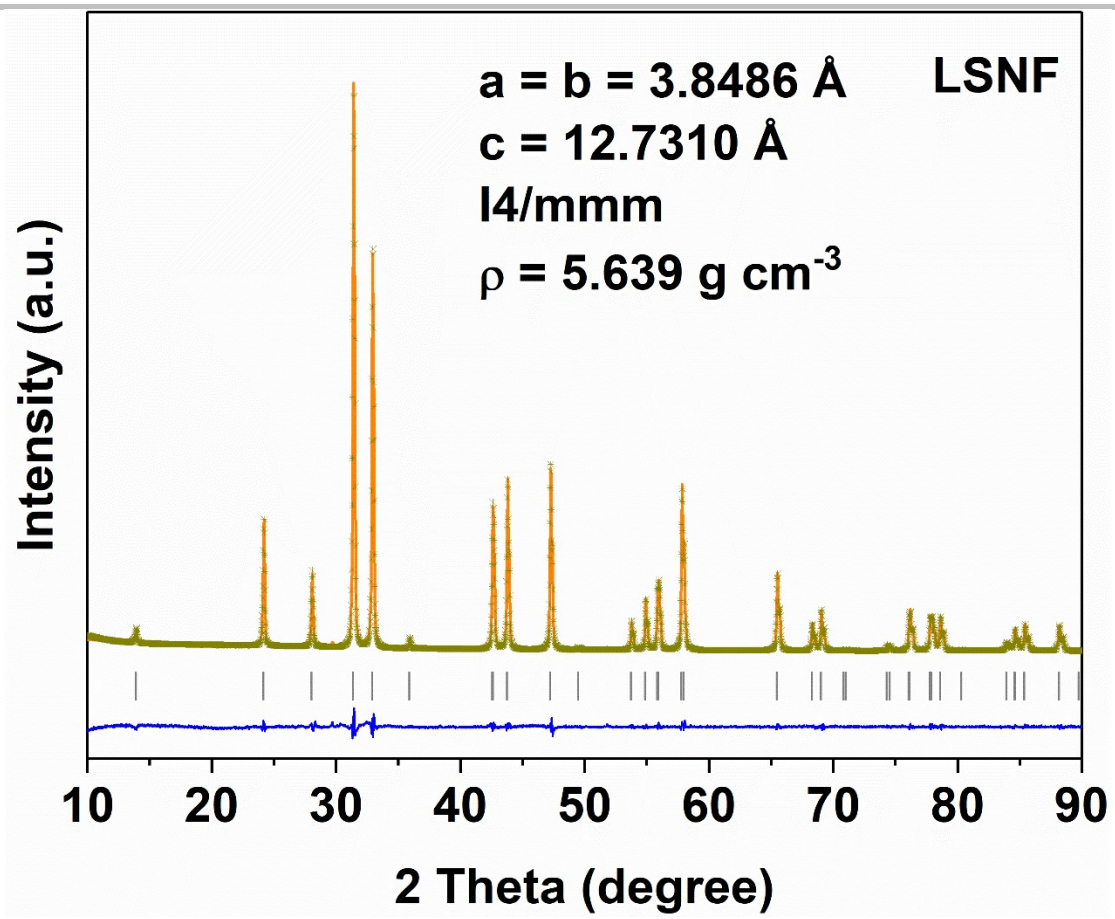

Figure S10. Rietveld refinement patterns. XRD refinement of the LSNF.

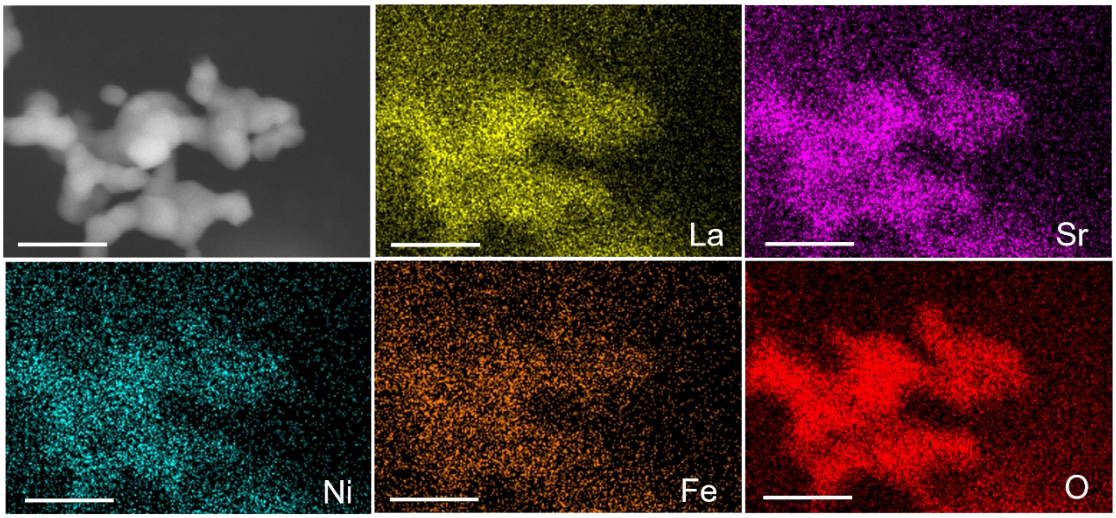

Figure S11. Elemental mappings of LSNF. The scale bar is 500 nm.

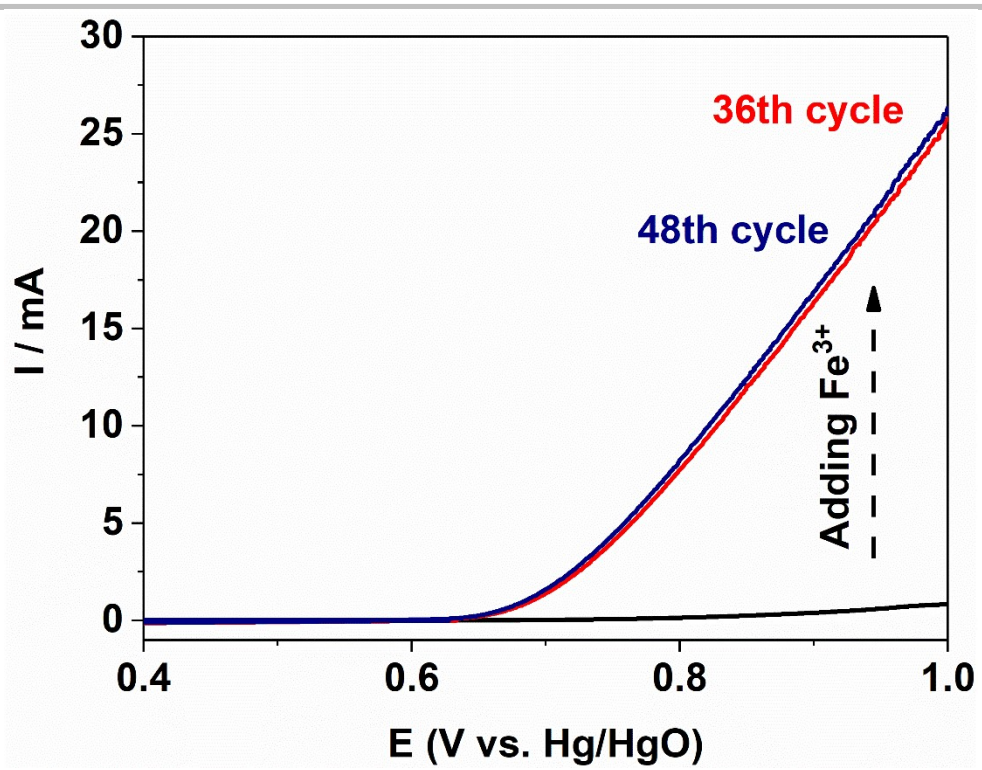

Figure S12. LSV plots. The 36th and 48th LSV of L_2N in 1.0 M KOH electrolyte containing Fe^{3+}. The potentials here are not corrected for iR.

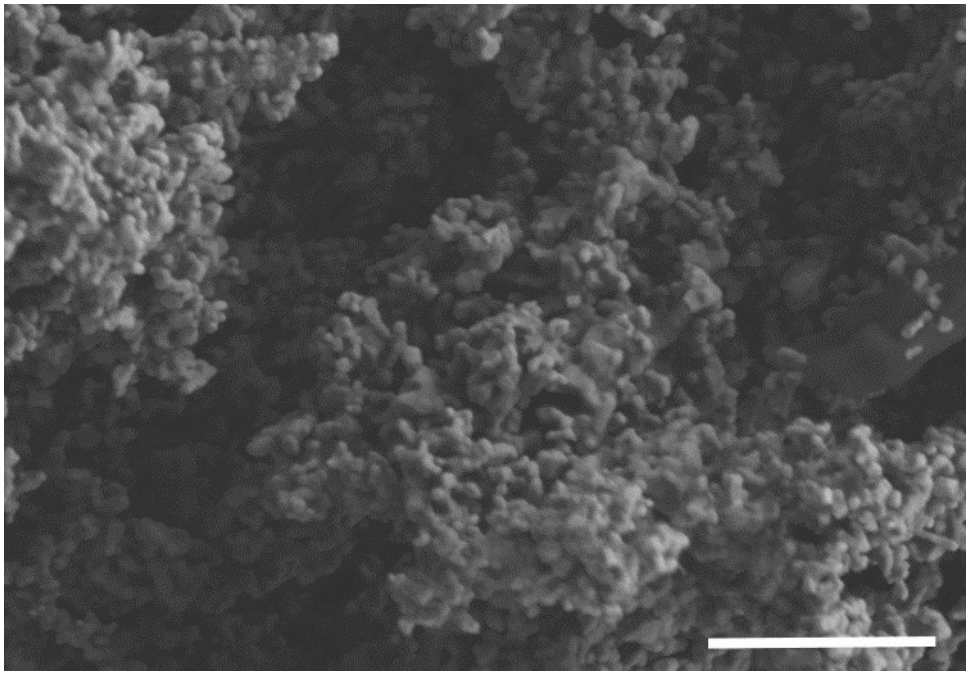

Figure S13. SEM images of L_2N-Fe. The scale bar is 3 μm.

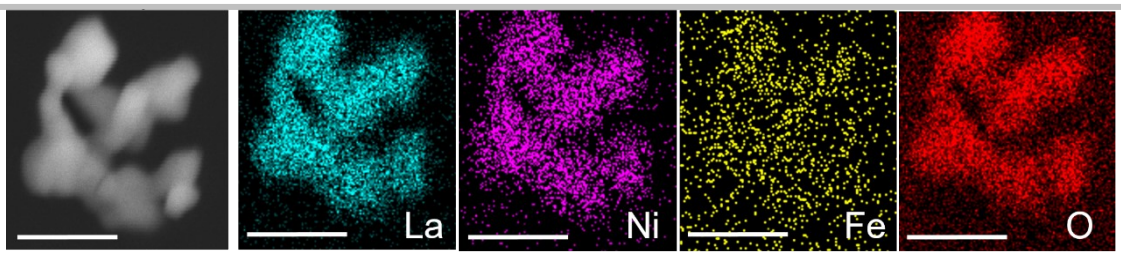

Figure S14. Elemental mappings of L_2N-Fe. The scale bar is 500 nm.

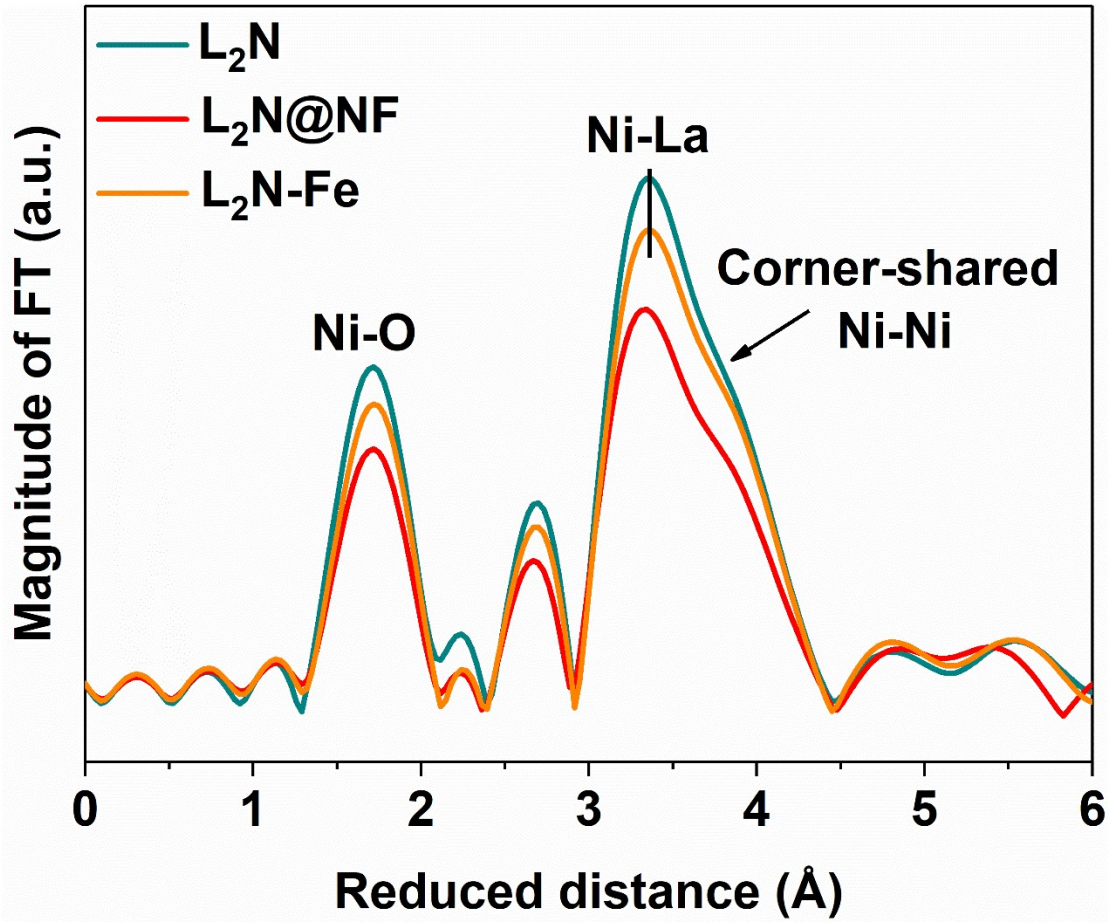

Figure S15. Fourier transform EXAFS. Ni K-edges of L_2N, L_2N@NF and L_2N-Fe samples. Although the peak intensities of Ni-O, Ni-La, and corner-sharing Ni-Ni in L_2N-Fe were slightly lower than those for the pristine L_2N, the Ni-La peak remained at the same position (approximately 3.4 Å), indicating that there were no detectable edge-sharing Ni-Fe pairs in the L_2N-Fe sample.

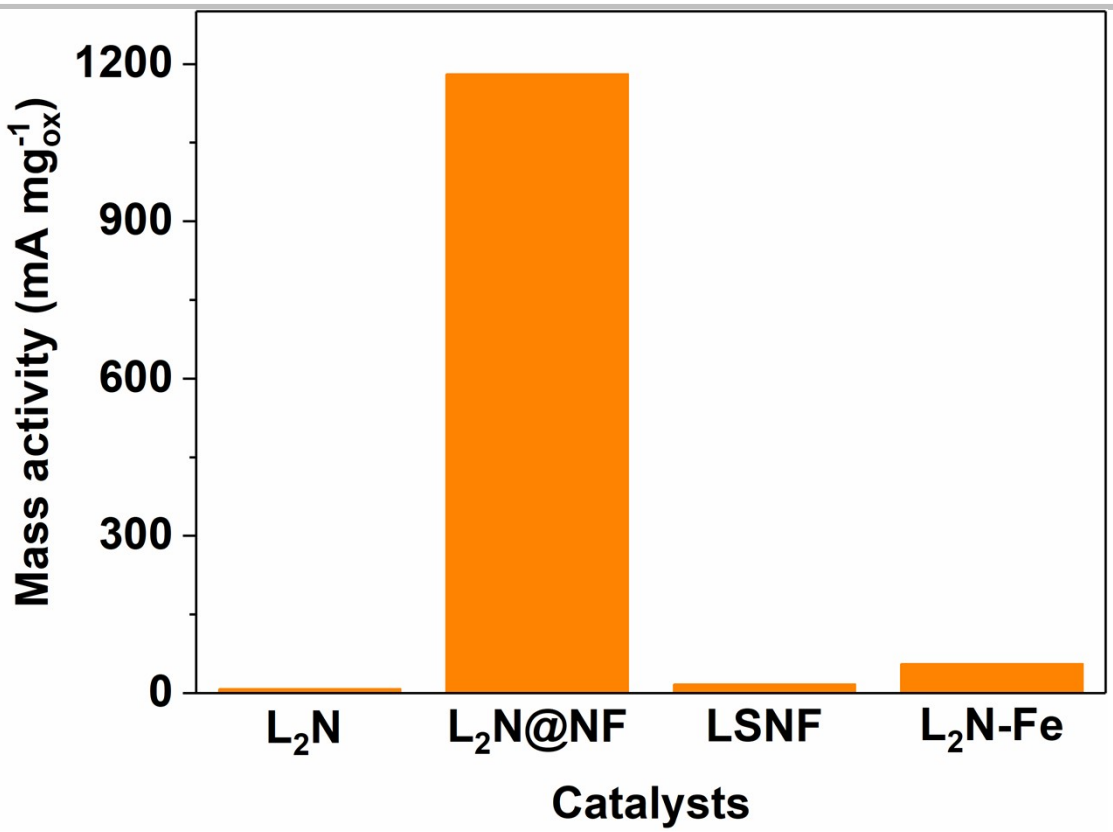

Figure S16. The mass activities. The mass activities of L_2N, L_2N@NF, LSNF and L_2N-Fe.

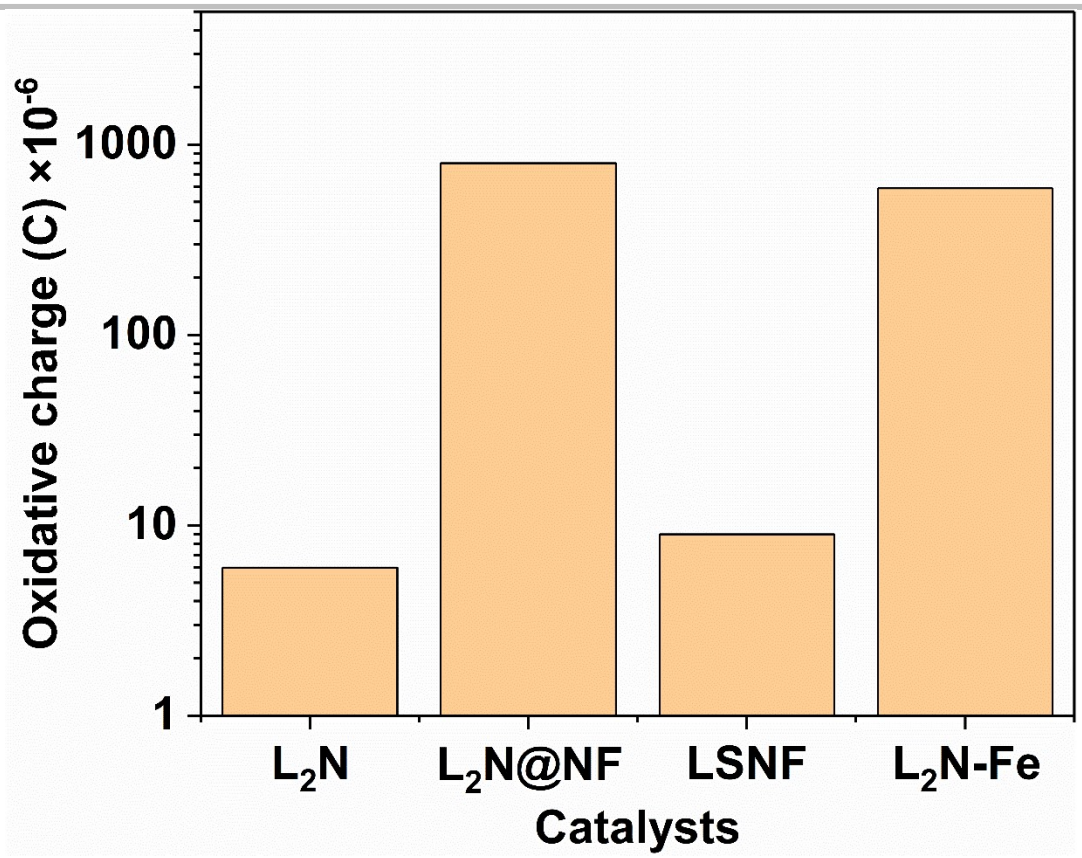

Figure S17. oxidative charge (C). oxidative charge of four samples obtained from the integration of oxidation waves. To facilitate the calculation of TOF, the charge unit here adopts Coulomb (C).

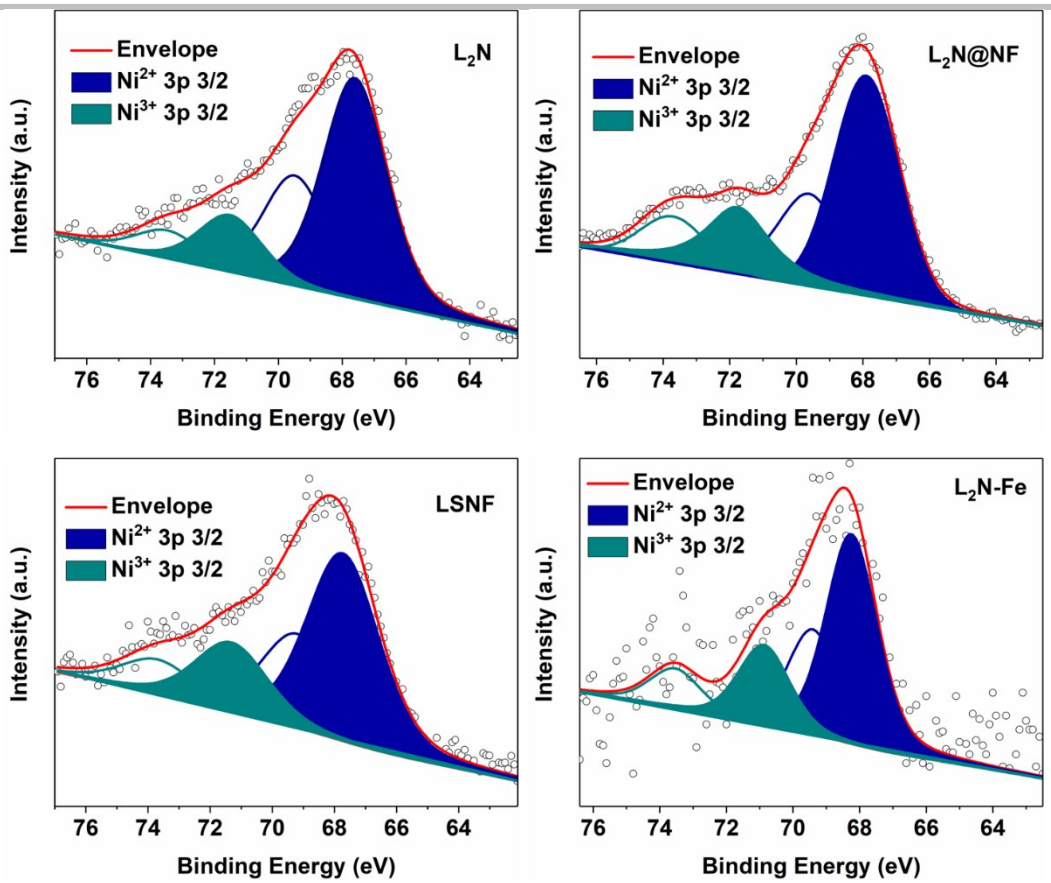

Figure S18. XPS analyze. XPS results for Ni 3p species on the surface of four samples. The Ni 3p spectrum was decomposed into 4 distinct components according to the previous methods developed by Burriel et. al.[1] The full peaks correspond to the 3p3/2 lines and the empty curves to the 3p1/2 lines. Ni^{2+} was marked in navy and Ni^{3+} was marked in dark cyan. All components used the same FWHM. The peak area of the Ni 3p1/2 was set up to have half area of their counterparts in the Ni 3p3/2.

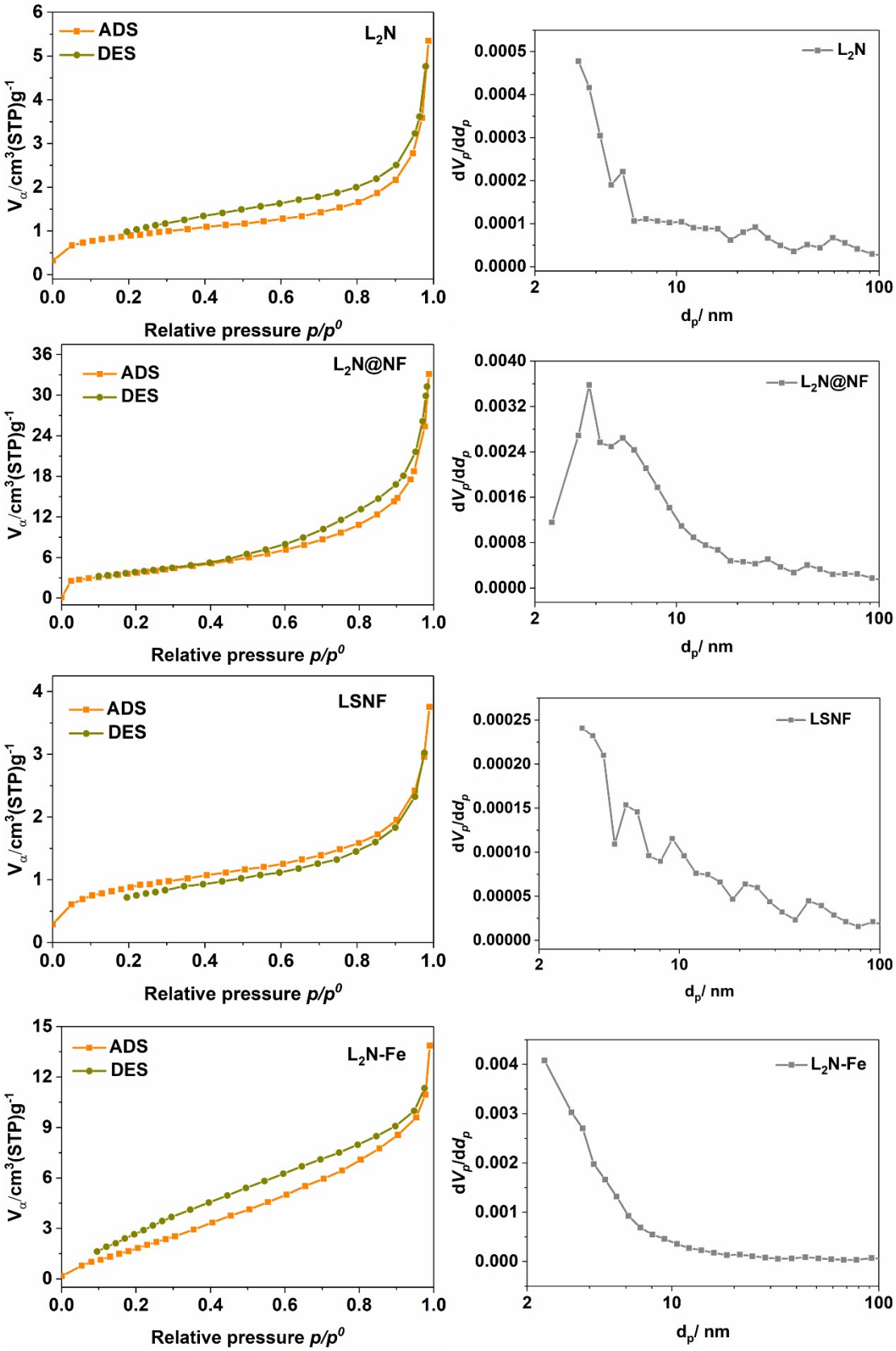

Figure S19. N_2 adsorption-desorption isotherms and pore distributions. The left four pictures are the typical N_2 adsorption-desorption isotherms of four samples, which can get the BET surface area. The right four pictures are the pore size analyze.

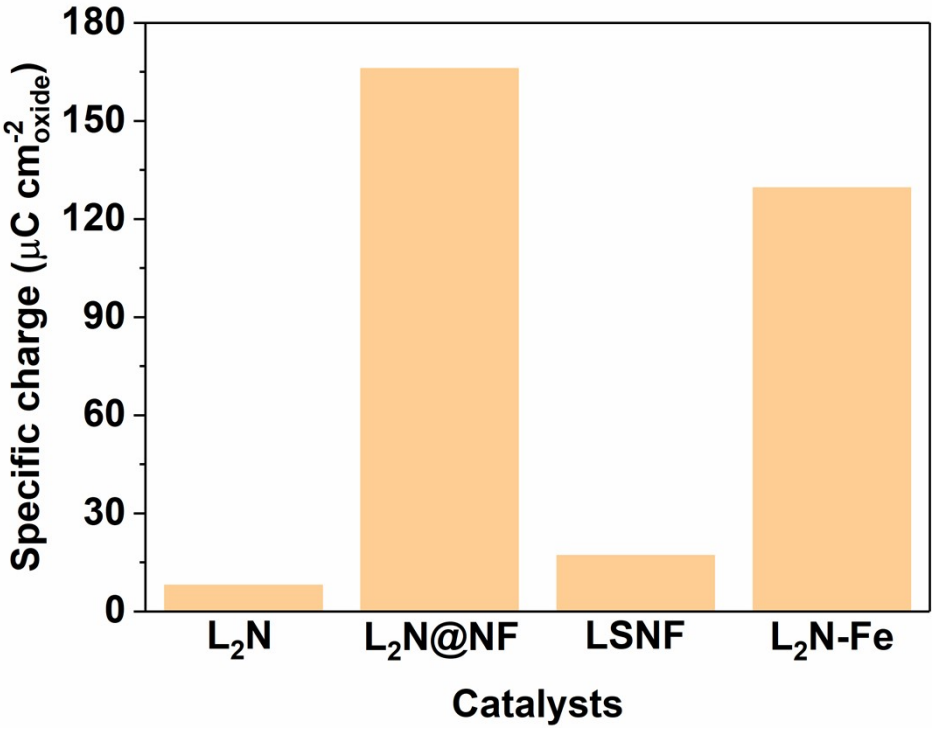

Figure S20. Specific oxidative charge (μC cm-2 oxide). Specific oxidative charge of four samples resulting from the integration of oxidation waves. The subscript oxide represents "the specific surface area of oxides measured by BET".

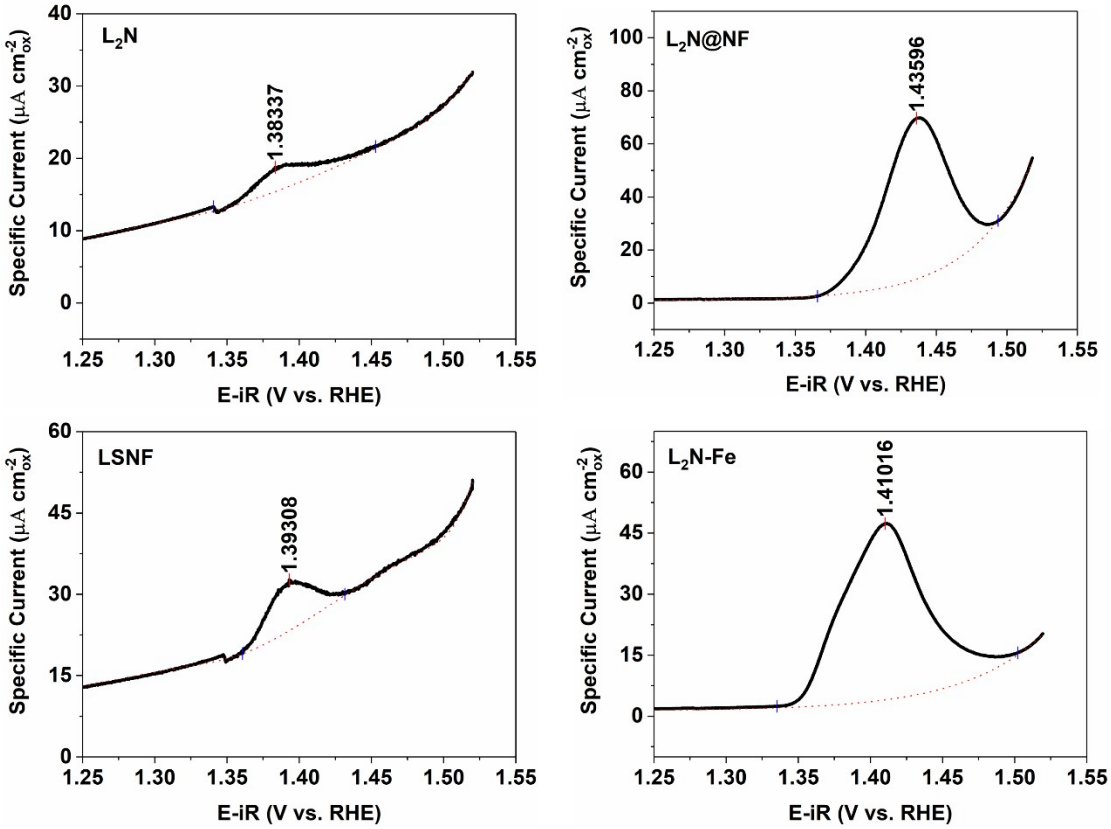

Figure S21. Fitted intercalation CVs for four samples. Integrating the region between the solid line and the red dotted line. The current is converted to the specific current according to the BET area.

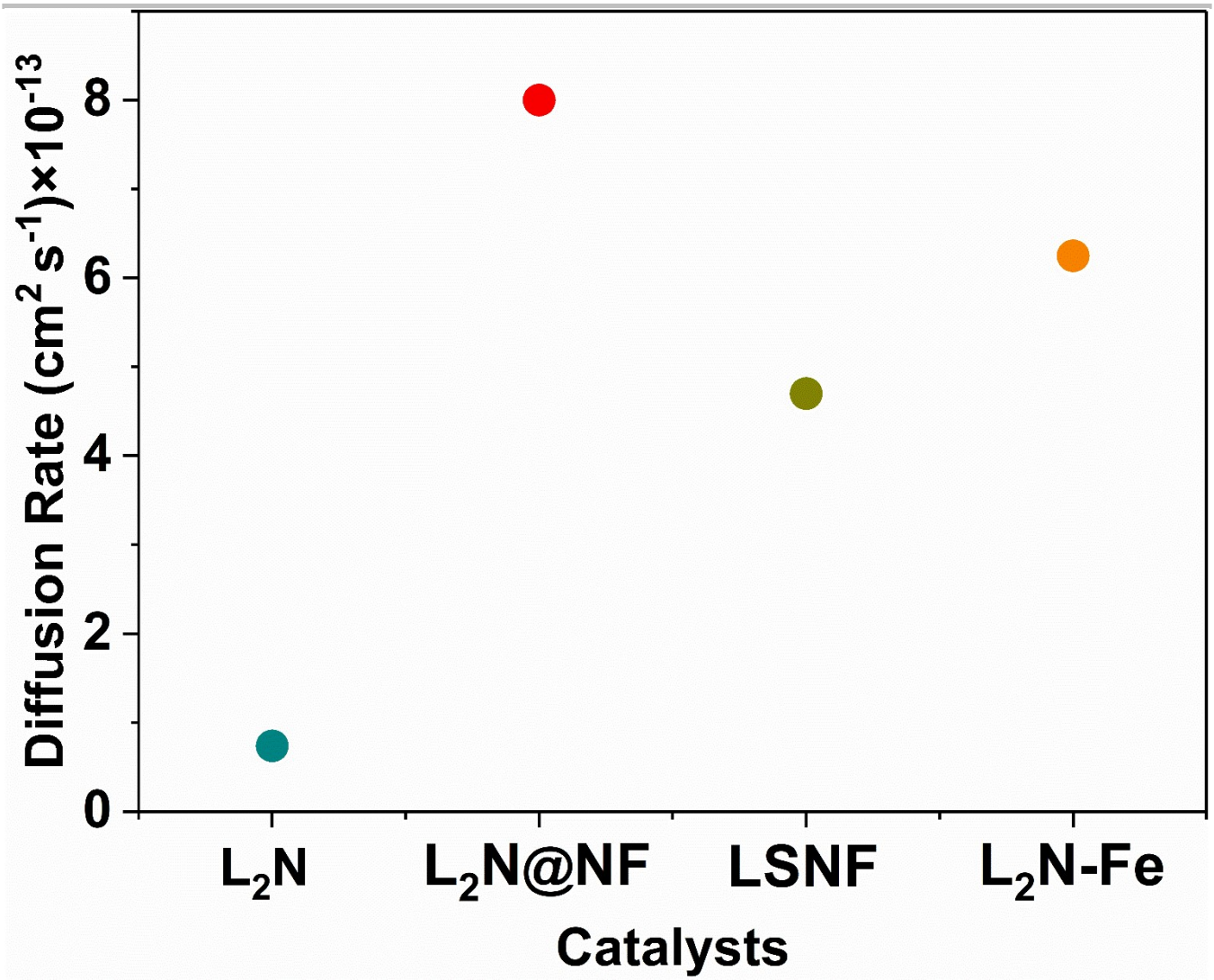

Figure S22. Oxygen ion diffusion coefficients. The diffusion rate was calculated from the chronoamperometry data. More details can be find in the section of Electrode preparation and electrochemical characterization.

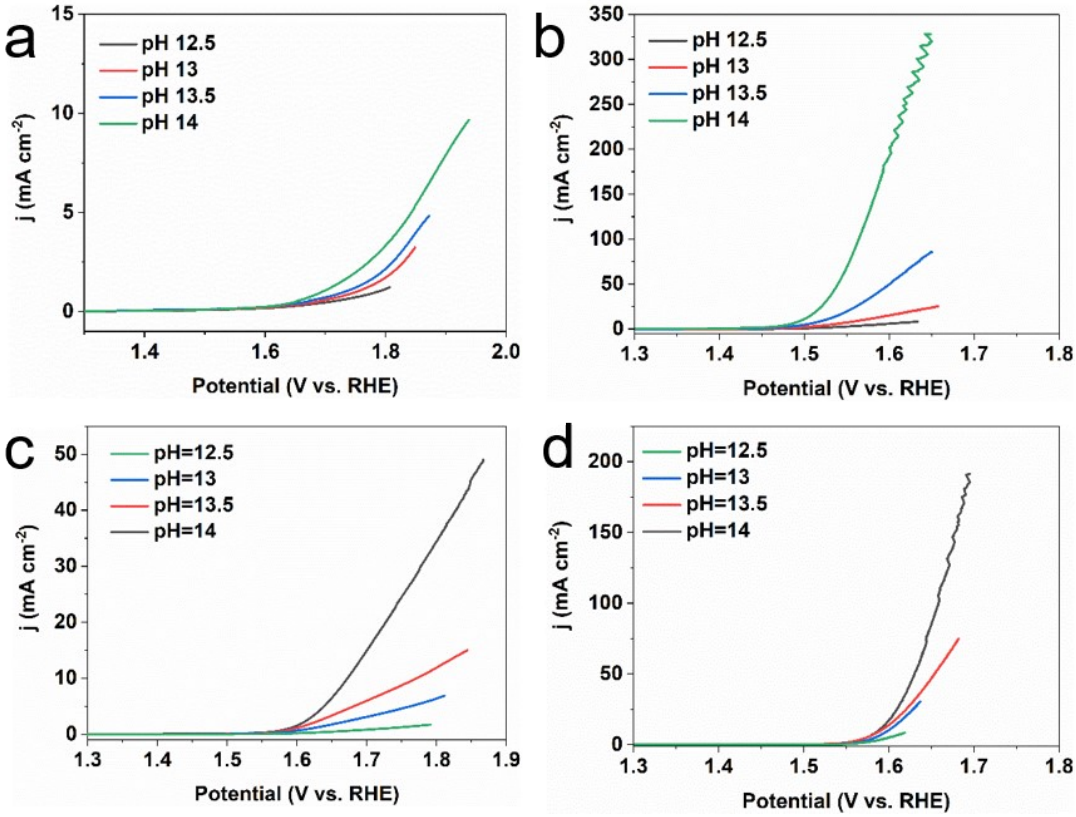

Figure S23. OER kinetic currents density. LSVs of **(a)** L_2N, **(b)** L_2N@NF, **(c)** LSNF and **(d)** L_2N-Fe in O_2-saturated KOH electrolytes with varying pH.

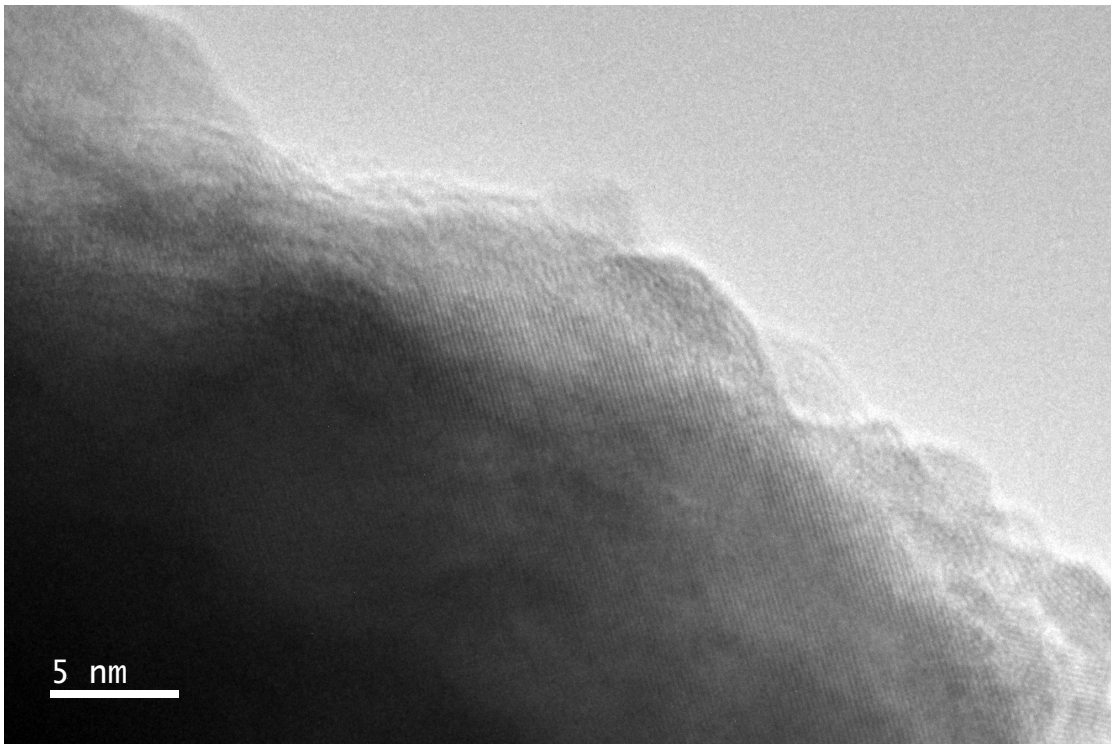

Figure S24. TEM image. The TEM image of L_2N@NF after the stability test.

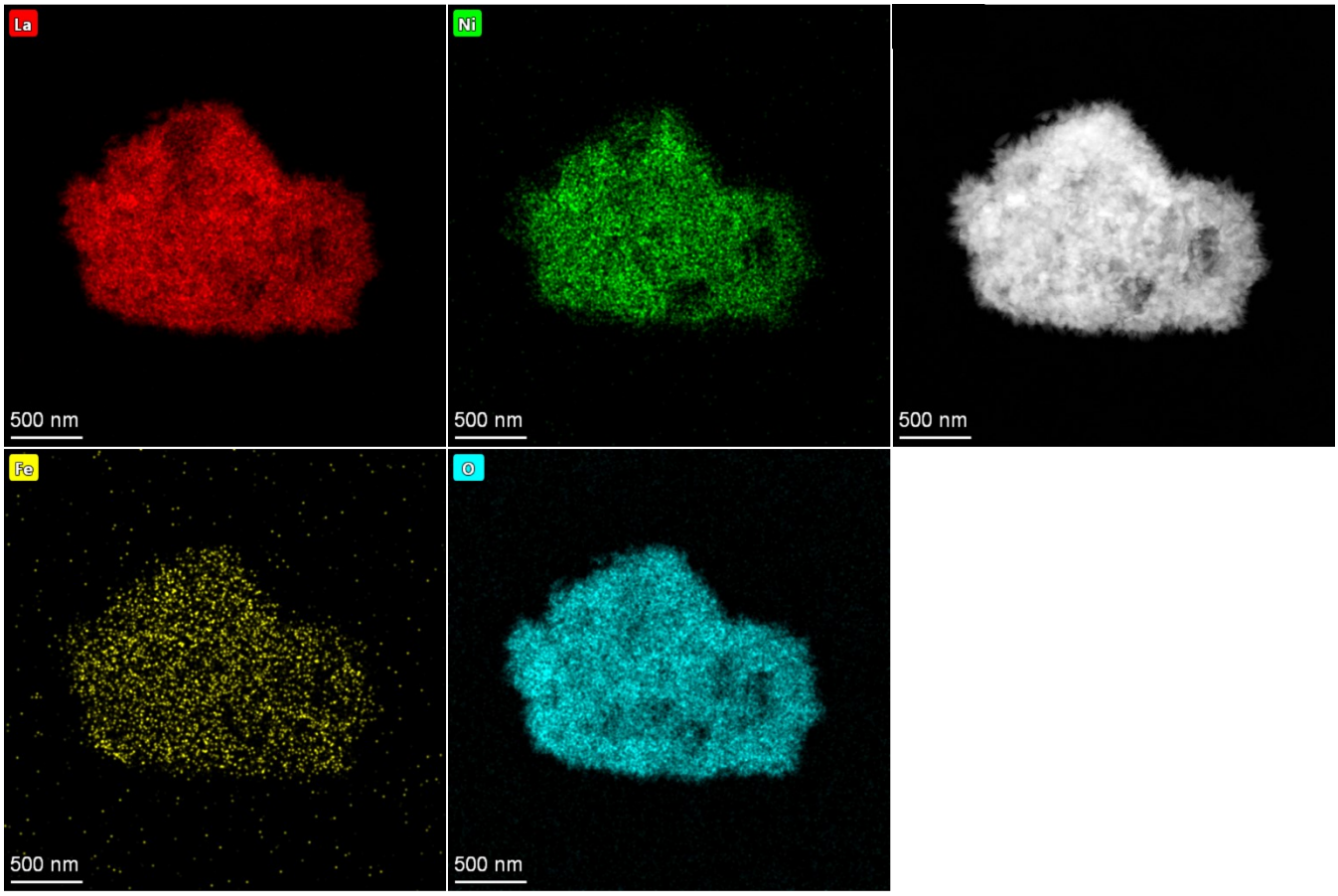

Figure S25. Elemental mappings. The elemental mapping of L_2N@NF after 60 h stability test.

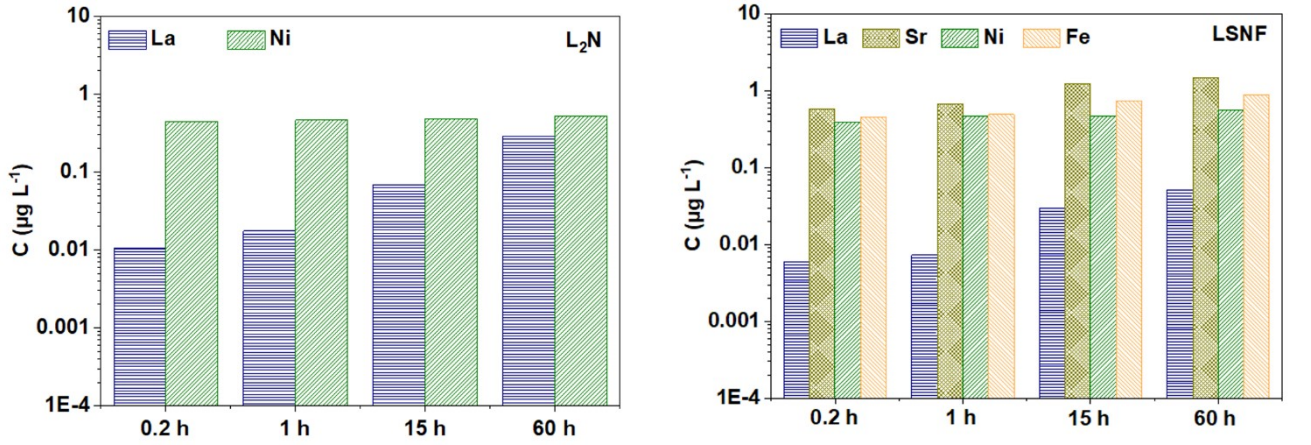

Figure S26. ICP-MS results. The dissolved metal concentration in the electrolyte of L_2N and LSNF at each sampling point from ICP-MS results.

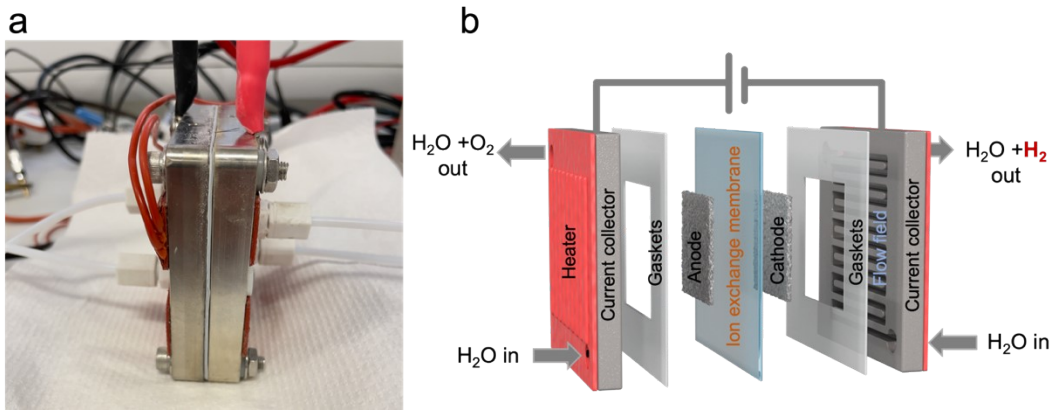

Figure S27. The optical image of the electrocatalyst system. (a) Digital photograph and (b) schematic of the anion exchange membrane electrolyzer.

Table S1. Comparison of the OER performance between the L_2N@NF catalyst and some state-of-the-art perovskite catalysts.

Catalysts	Substrate	Electrolyte	η_{10} (mV)	Tafel slope (mV dec^{-1})	Reference
L_2N@NF	GCE	1 M KOH	258	54	This work
LSNF30	GCE	0.1M KOH	~365	44	2
RP-SCFN	GCE	0.1M KOH	334	57	3
La_2CoO_4	GCE	0.1M KOH	400	64	4
PBSCF0.45	GCE	1 M KOH	290	69	5
RP/P-LSCF	GCE	0.1M KOH	324	58	6
RP-$LaSr_3(Co_{0.5}Fe_{0.5})_3O_{10-\delta}$	GCE	0.1M KOH	388	83.9	7
$La_5Ni_3CoO_{13-\delta}$	GCE	0.1M KOH	370	35	8
$La_4Ni_3O_{10.26}$	GCE	0.1M KOH	480(η_1)	142	9
$H_{3.6}IrO_4 \cdot 3.7H_2O$	GCE	0.1 M $HClO_4$	~270	/	10
$SmBaCo_{1.5}Mn_{0.5}O_{5+\delta}$	pellets	1 M KOH	310	/	11
LSCN8264	GCE	1 M KOH	290	/	12
BSCFI-91	GCE	1 M KOH	300	61.2	13
LFNO-II NRs	GCE	1 M KOH	302	50	14
LNMO-1	GCE	1 M KOH	370	58	15
SNCF-NRs	GCE	0.1M KOH	390	61	16
$La_2Li_{0.5}Ni_{0.5}O_4$	GCE	0.1M KOH	~410(η_1)	90	17
NiO-$(La_{0.613}Ca_{0.387})_2NiO_{3.562}$	GCE	0.1M KOH	373	42	18
NMP-treated $Sr_3FeCoO_{7-\delta}$	GCE	1 M KOH	343	63	19
LSN-03	GCE	0.1M KOH	~520($\eta_{0.8}$)*	/	20
$La_3SrNi_3O_{10}$	GCE	0.1M KOH	500	89	21
r-LSCF-P	GCE	0.1M KOH	350	64	22
LP-$LaSr_3Co_{1.5}Fe_{1.5}O_{10-\delta}$	GCE	0.1M KOH	388	83.9	23
BCTO	GCE	0.1M KOH	470	87	24
$Bi_4Ti_3O_{12} \cdot (BiCoO_3)_2$	GCE	1 M NaOH	320	34	25
$Sr_3Co_2O_5Cl_2$	GCE	1 M KOH	350	62	26
OP-SLNO	GCE	0.1M KOH	490	151.4	27
$Sr_3Ir_2O_7$	GCE	1 M KOH	296	53	28
		0.5 M H_2SO_4	259	50	
Sr_2IrO_4	GCE	0.5 M H_2SO_4	360($\eta_{50.4}$)[a]	/	29
Sr_2IrO_4	GCE	0.1 M $HClO_4$	290	45/73[b]	30
		0.5 M H_2SO_4	291	40/120[b]	

*: Ohmic potential drop was not compensated for in this measurement.

a: The current density 50.4 mA cm^{-2}_{disk} was calculated from the article data. The overpotential 360 mV was also higher than our results at the current density of 50.4 mA $cm^{-2}_{disk.}$

b: The numbers before and after indicated Tafel slope fitted at low current densities and high current densities, respectively.

Table S2. Chemical composition of the L_2N and L_2N@NF samples.

Catalysts	La (mg L^{-1})	Ni (mg L^{-1})	Fe (mg L^{-1})	Composition ratio
L_2N	36.43	7.989	/	$La_{1.93}NiO_4$
L_2N@NF	20.02	4.792	1.684	$La_{0.1441}Ni_{0.0816}Fe_{0.03015}$

Table S3. Surface atomic concentration from XPS.

Catalysts	La (Sr)	Ni	Fe
L_2N	83.05%	16.95%	/
L_2N@NF	49.31%	24.66%	26.03%
LSNF	76.66%	13.27%	10.07%
L_2N-Fe	52.88%	2.46%	44.66%

The surface element content of LSNF and L_2N-Fe measured by XPS also proved the successful application of our surface tailoring strategy. The approximate element ratio of La (Sr)/Ni/Fe on LSNF and L_2N surfaces indicates the La/Sr-terminal of LSNF. Nearly half of the Fe content on L_2N-Fe surface indicates a large deposition of Fe. Furthermore, the amount of La on L_2N-Fe surface was reduced to almost half, which may be part of La wrapped in Ni/Fe during the 40-cycle LSVs.

Table S4. Comparison of the OER intrinsic activity between the L_2N@NF catalyst and some well-known NiFe catalysts.

Catalysts	TOF(s^{-1}) @300mV	Electrolyte	η_{10} (mV)	Tafel slope (mV dec^{-1})	Reference
L_2N@NF	1.8	1 M KOH	258	54	This work
F-NiFe-A	0.25±0.03	1M KOH	218	31	31
S-NiCoFe LDH/CC	0.102	1M KOH	206	48	32
NiFe-LDH HMS/NF	0.206	1M KOH	239	53	33
NiO/NiFe LDH	0.71	1 M KOH	274(η_{100})	30	34
Fe^{2+} - NiFe LDH	0.09	1M KOH	249	40.3	35
$Ni_{0.67}Fe_{0.33}$/C	0.3	1M KOH	210	35.1	36
FeNi LDH	0.028	1M KOH	232	48	37
$Ni(Fe)O_xH_y$	~0.75	1M KOH	/	/	38
$Ni_{0.75}Fe_{0.25}OOH$	9(η_{350})	1M KOH	/	/	39
$Ni_{45}Fe_{55}$	0.14	0.1 M KOH	~310	35	40
Ni_{65}+Fe_{35} p.m.	0.1	0.1 M KOH	298	37	41
Ni_2Fe_1/C	1.04	1 M KOH	250	/	42
$Ni_{2/3}Fe_{1/3}$-rGO	0.1	1 M KOH	210	40	43
Ultrathin LDH	0.14577	1 M KOH	210	31	44
Ni_8Fe-LDH@CNTs	0.35	1M KOH	220	34	45
FeNi-rGO LDH	0.987	0.1M KOH	~205	39	46

Table S5. Specific surface areas of four samples measured by nitrogen adsorption testing using the BET method.

Catalysts	S(m^2 g^{-1})	Pore volume(cm^3 g^{-1})
L_2N	1.65	0.006747
L_2N@NF	13.6	0.051236
LSNF	1.16	0.004862
L_2N-Fe	10.8	0.023367

Table S6. MEA stability and the corresponding test conditions of some state-of-the-art electrocatalysts.

Catalysts (anode//cathode)	Stability	Current density (mA cm^{-2})	Temperature (℃)	Membrane	Ref.
L_2N@NF//Pt/C	300 h	200	60	Sustanion X37-50 grade RT	This work
IrO_2//Pt/C	34 h	200	60	Sustanion X37-50 grade RT	This work
Fe-NiMoNH_3/H_2//NiMo-NH_3/H_2	25 h	500	20	Sustanion X37-50 grade T	47
BSCF-FS//Pt/C	5 h	200	50	Tokuyama supplied A201	48
$(NiCo)_3Se_4$//Pt/C	First segment 50h	1000	25	Sustanion X37-50	49
$(NiCo)_3Se_4$//Pt/C	Second segment 40h	1000	60	Sustanion X37-50	49
NiFe nanofoam//PtRu/C	170 h	200	60	HTMA-DAPP	50
$NiCoFeO_x$//Pt/C	180 h	200	50	FAA-3	51

References

1 M. Burriel, S. Wilkins, J.P. Hill, M.A. Muñoz-Márquez, H.H. Brongersma, J.A. Kilner, M.P. Ryan and S.J. Skinner, *Energy Environ. Sci.,* 2014, **7**, 311-316.

2 R.P. Forslund, W.G. Hardin, X. Rong, A.M. Abakumov, D. Filimonov, C.T. Alexander, J.T. Mefford, H. Iyer, A.M. Kolpak, K.P. Johnston and K.J. Stevenson, *Nat. Commun.,* 2018, **9**, 3150.

3 Y. Zhu, H.A. Tahini, Z. Hu, Y. Yin, Q. Lin, H. Sun, Y. Zhong, Y. Chen, F. Zhang, H.-J. Lin, C.-T. Chen, W. Zhou, X. Zhang, S.C. Smith, Z. Shao and H. Wang, *EcoMat.,* 2020, **2**, e12021.

4 B. Yin, Y. Li, N. Sun, X. Ji, Y. Huan, D. Dong, X. Hu and T. Wei, *Electrochim. Acta.,* 2021, **370**, 137747.

5 H. Jo, Y. Yang, A. Seong, D. Jeong, J. Kim, S.H. Joo, Y.J. Kim, L. Zhang, Z. Liu, J.-Q. Wang, S.K. Kwak and G.

Kim, *J. Mater. Chem. A,* 2022, **10**, 2271-2279.
6 Y. Zhu, Q. Lin, Z. Hu, Y. Chen, Y. Yin, H.A. Tahini, H.-J. Lin, C.-T. Chen, X. Zhang, Z. Shao and H. Wang, *Small.,* 2020, **16**, 2001204.
7 S. Liu, C. Sun, J. Chen, J. Xiao and J.-L. Luo, *ACS catal.,* 2020, **10**, 13437-13444.
8 S.R. Choi, J.-I. Lee, H. Park, S.W. Lee, D.Y. Kim, W.Y. An, J.H. Kim, J. Kim, H.-S. Cho and J.-Y. Park, *Chem. Eng. J.,* 2021, **409**, 128226.
9 J. Yu, J. Sunarso, Y. Zhu, X. Xu, R. Ran, W. Zhou and Z. Shao, *Chem. Eur. J.,* 2016, **22**, 2719-2727.
10 R. Zhang, P.E. Pearce, V. Pimenta, J. Cabana, H. Li, D. Alves Dalla Corte, A.M. Abakumov, G. Rousse, D. Giaume, M. Deschamps and A. Grimaud, *Chem. Mater.,* 2020, **32**, 3499-3509.
11 A. Olszewska, K. Świerczek and A. Niemczyk, *Crystals.,* 2020, **10**, 205.
12 J. Cheng, Z. Wang, L. Zou, M. Zhang, G. Zhang, Y. Dong, Y. Jiang, Y. Huang, N. Nakashima and B. Chi, *J. Alloy. Compd.,* 2020, **831**, 154728.
13 Q. Luo, D. Lin, W. Zhan, W. Zhang, L. Tang, J. Luo, Z. Gao, P. Jiang, M. Wang, L. Hao and K. Tang, *ACS Appl. Energy Mater.,* 2020, **3**, 7149-7158.
14 H. Wang, J. Wang, Y. Pi, Q. Shao, Y. Tan and X. Huang, *Angew. Chem. Int. Ed.,* 2019, **58**, 2316-2320.
15 Y. Tong, J. Wu, P. Chen, H. Liu, W. Chu, C. Wu and Y. Xie, *J. Am. Chem. Soc.,* 2018, **140**, 11165-11169.
16 Y. Zhu, W. Zhou, Y. Zhong, Y. Bu, X. Chen, Q. Zhong, M. Liu and Z. Shao, *Adv. Energy Mater.,* 2017, **7**, 1602122.
17 C. Yang, M. Batuk, Q. Jacquet, G. Rousse, W. Yin, L. Zhang, J. Hadermann, A.M. Abakumov, G. Cibin, A. Chadwick, J.-M. Tarascon and A. Grimaud, *ACS Energy Lett.,* 2018, **3**, 2884-2890.
18 R. Liu, F. Liang, W. Zhou, Y. Yang and Z. Zhu, *Nano Energy.,* 2015, **12**, 115-122.
19 K. Xu, F. Song, J. Gu, X. Xu, Z. Liu and X. Hu, *J. Mater. Chem. A,* 2018, **6**, 14240-14245.
20 K.-N. Jung, J.-H. Jung, W.B. Im, S. Yoon, K.-H. Shin and J.-W. Lee, *ACS Appl. Mater. Interfaces,* 2013, **5**, 9902-9907.
21 C. Cao, C. Shang, X. Li, Y. Wang, C. Liu, X. Wang, S. Zhou and J. Zeng, *Nano Lett.,* 2020, **20**, 2837-2842.
22 C. Li, Y. Wang, C. Jin, J. Lu, J. Sun and R. Yang, *Int. J. Hydrogen Energy.,* 2020, **45**, 22959-22964.
23 S. Liu, H. Luo, Y. Li, Q. Liu and J.-L. Luo, *Nano Energy.,* 2017, **40**, 115-121.
24 X. Li, Y. Sun, Q. Wu, H. Liu, W. Gu, X. Wang, Z. Cheng, Z. Fu and Y. Lu, *J. Am. Chem. Soc.,* 2019, **141**, 3121-3128.
25 X. Li, H. Liu, Z. Chen, Q. Wu, Z. Yu, M. Yang, X. Wang, Z. Cheng, Z. Fu and Y. Lu, *Nat. Commun.,* 2019, **10**, 1409.
26 Y. Miyahara, K. Miyazaki, T. Fukutsuka and T. Abe, *Chem. Commun.,* 2017, **53**, 2713-2716.
27 H. Kim, Y.S. Lim and J.H. Kim, *Chem. Eng. J.,* 2022, **431**, 134278.
28 C. Zhu, H. Tian, B. Huang, G. Cai, C. Yuan, Y. Zhang, Y. Li, G. Li, H. Xu and M.-R. Li, *Chem. Eng. J.,* 2021, **423**, 130185.
29 C.W. Song, J. Lim, H.B. Bae and S.-Y. Chung, *Energy Environ. Sci.,* 2020, **13**, 4178-4188.
30 A.L. Strickler, D. Higgins and T.F. Jaramillo, *ACS Appl. Energy Mater.,* 2019, **2**, 5490-5498.
31 Q. Xu, H. Jiang, X. Duan, Z. Jiang, Y. Hu, S. W. Boettcher, W. Zhang, S. Guo and C. Li, *Nano Lett.,* 2021, **21**, 492-499.
32 L.M. Cao, J.W. Wang, D.C. Zhong and T.B. Lu, *J. Mater. Chem. A,* 2018, **6**, 3224.
33 C. Zhang, M. Shao, L. Zhou, Z. Li, K. Xiao and M. Wei, *ACS Appl. Mater. Interfaces*, 2016, **8**, 33697-33703.

34 Z. W. Gao, J. Y. Liu, X. M. Chen, X. L. Zheng, J. Mao, H. Liu, T. Ma, L. Li, W.C. Wang and X.W. Du, *Adv. Mater.*, 2019, **31**, 1804769.

35 Z. Cai, D. Zhou, M. Wang, S.-M. Bak, Y. Wu, Z. Wu, Y. Tian, X. Xiong, Y. Li, W. Liu, S. Siahrostami, Y. Kuang, X,-Q. Yang, H. Duan, Z. Feng, H. Wang and X. Sun, *Angew. Chem. Int. Ed.*, 2018, **57**, 9392-9396.

36 S. Yin, W. Tu, Y. Sheng, Y. Du, M. Kraft, A. Borgna and R. Xu, *Adv. Mater.*, 2018, **30**, 1705106.

37 X. Long, J. Li, S. Xiao, K. Yan, Z. Wang, H. Chen and S. Yang, *Angew. Chem.,* 2014, **126**, 7714-7718.

38 M.B. Stevens, C.D.M. Trang, L.J. Deng and S.W. Boettcher, *J. Am. Chem. Soc.,* 2017, **139**, 11361-11364.

39 S. Zou, M.S. Burke, M.G. Kast, J. Fan, N. Danilovic and S.W. Boettcher, *Chem. Mater.,* 2015, **27**, 8011-8020.

40 M. Görlin, P. Chernev, J.F. de Araújo, T. Reier, S. Dresp, B. Paul, R. Krähnert, H. Dau and P. Strasser, *J. Am. Chem. Soc.,* 2016, **138**, 5603-5614.

41 M. Görlin, P. Chernev, P. Paciok, C.-W. Tai, J.F. de Araújo, T. Reier, M. Heggen, R. Dunin-Borkowski, P. Strasser and H. Dau, *Chem. Commun.,* 2019, **55**, 818-821.

42 Y.-J. Ko, M.H. Han, H. Kim, J.-Y. Kim, W.H. Lee, J. Kim, J.Y. Kwak, C.-H. Kim, T.-E. Park, S.-H. Yu, W.-S. Lee, C.H. Choi, P. Strasser and H.-S. Oh, *Chem Catalysis,* 2022, **2**, 2312-2327.

43. W. Ma, R. Ma, C. Wang, J. Liang, X, Liu, K. Zhou and T. Sasaki, *ACS Nano*, 2015, **9**, 1977-1984.

44 C. Kuai, Y. Zhang, D. Wu, D. Sokaras, L. Mu, S. Spence, D. Nordlund, F. Lin and X.-W. Du, *ACS Catal.*, 2019, **9**, 6027-6032.

45 D. Zhao, K. Jiang, Y. Pi, and X. Huang, *ChemCatChem*, 2017, **9**, 84-88.

46 X. Long, J. Li, S. Xiao, K. Yan, Z. Wang, H. Chen and S. Yang, *Angew. Chem. Int. Ed.,* 2014, **53**, 7584-7588.

47 P. Chen and X. Hu, *Adv. Energy Mater.,* 2020, **10**, 2002285.

48 E. Fabbri, M. Nachtegaal, T. Binninger, X. Cheng, B.-J. Kim, J. Durst, F. Bozza, T. Graule, R. Schäublin, L. Wiles, M. Pertoso, N. Danilovic, K.E. Ayers and T.J. Schmidt, *Nat. Mater.,* 2017, **16**, 925-931.

49 J. Abed, S. Ahmadi, L. Laverdure, A. Abdellah, C.P. O'Brien, K. Cole, P. Sobrinho, D. Sinton, D. Higgins, N. J. Mosey, S.J. Thorpe and E.H. Sargent, *Adv. Mater.,* 2021, **33**, 2103812.

50 D. Li, E.J. Park, W. Zhu, Q. Shi, Y. Zhou, H. Tian, Y. Lin, A. Serov, B. Zulevi, E.D. Baca, C. Fujimoto, H.T. Chung and Y.S. Kim, *Nat. Energy.,* 2020, **5**, 378-385.

51 D. Xu, M.B. Stevens, M.R. Cosby, S. Z. Oener, A.M. Smith, L.J. Enman, K.E. Ayers, C.B. Capuano, J.N. Renner, N. Danilovic, Y. Li, H. Wang, Q. Zhang and S.W. Boettcher, *ACS Catal.,* 2019, **9**, 7-15.